Modeling Urban Land Surface Temperature Using Physics-Informed Neural Networks (PINNs)

Ronak Ghanbari [1*], Marc Linderman [2], Hossein Arefi [3], Hossein Torabzadeh [1], Morteza Heidari Mozaffar [1]

[1] Dept. of Civil Engineering, Bu Ali Sina University, Hamedan, Iran (r.ghanbari, torabzadeh, m.heidarimozaffar)@basu.ac.ir
[2] Dept. of Geographical and Sustainability Sciences, University of Iowa, 316 Jessup Hall, Iowa City, IA 52242, USA -marc-linderman@uiowa.edu
3 i3mainz, Institute for Spatial Information and Surveying Technology, Mainz University of Applied Sciences, 55128 Mainz, Germany - hossein.arefi@hs-mainz.de

KEY WORDS: Land Surface Temperature (LST), Landsat-8, Urban Heat Island (UHI), Physics-Informed Neural Network (PINN), Spectral Indices, Meteorological Variables.

ABSTRACT

A compact physics-informed neural network (PINN) is developed to (i) quantify city-scale accuracy of 30 m urban land surface temperature (LST) maps, (ii) identify influential predictors, and (iii) contrast climate-dependent patterns between New York City (NYC) (humid to sub-humid) and Austin, Texas (humid subtropical). Inputs combine selected Landsat-8 spectral indices, a digital elevation model, and meteorological covariates. LST targets are retrieved from Landsat-8 thermal band 10 (single-channel), quality-screened, and resampled to 30 m for May–September 2023. The loss combines data mean squared error term with a lightweight temporal smoothness prior implemented as a finite-difference term ($\Delta T/\Delta t$) on same-pixel pairs to reflect heat storage behaviour and discourage unrealistically rapid day to day changes. On the study pixels (in-sample), performance reaches $R^2 = 0.88$ (RMSE = 1.2 °C) in NYC and $R^2 = 0.91$ (RMSE = 0.9 °C) in Austin; errors are approximately Gaussian with minimal bias. Feature patterns differ by climate: vegetation-related signals dominate cooling in NYC, whereas shortwave-radiation and impervious-surface proxies (e.g., NDBI/NDISI) are strongest in Austin. These findings show that a shallow PINN with a minimal temporal constraint yields accurate, interpretable LST maps suitable for urban-heat-island assessment and climate-sensitive heat-mitigation planning.

1. INTRODUCTION

Urbanization raises land-surface temperature (LST) and fosters urban heat islands (UHIs) through changes in land use and surface properties. Accurate LST estimation is essential for assessing thermal conditions and planning climate-adaptation measures. Conventional Landsat retrievals (e.g., single-channel; split-window on other sensors) are grounded in radiative-transfer assumptions but remain sensitive to emissivity specification, atmospheric correction, BRDF effects, and mixed pixels, which can limit robustness across different climates(Qin et al. 2001; Sobrino et al. 2004; Weng, 2009). Data-driven frameworks have gained traction as complements to conventional retrievals. They capture complex patterns but often require substantial labelled data and typically do not encode governing physics (e.g., heat-storage behaviour), which may limit portability across different climates. Recent studies have examined deep and hybrid learning for UHI/LST modeling (Zhu et al. 2021; Tehrani et al. 2024), consistently showing that vegetation and built-environment indices strongly influence LST dynamics (Weng et al. 2004; Zhou et al. 2014; Zhou WeiQi et al. 2017).

Additional evidence highlights the roles of urban morphology, topographic and land-cover factors, and albedo: Landsat- and climate-informed analyses of morphology (Zhao et al. 2020), city-scale studies in Asia emphasizing topography and land cover regression models that include road-network density and albedo (Dai et al. 2018) and work combining morphological features with spectral indices(Ghanbari, Heidarimozaffar, Soltani and Arefi, 2023) . At inter-city/supra-urban scales, cross-city comparisons of GRU/ANN/DNN indicate the feasibility of large-scale UHI modeling under diverse urban forms (Tehrani et al. 2024). In a separate case, a CNN framework for Paris (2004–2022) improved mapping of LST and 2-m air temperature relative to ERA5 and captured extremes more faithfully (Johannsen et al. 2024).

Together, these findings motivate hybrid strategies that retain physical plausibility without sacrificing efficiency setting the stage for the physics-informed approach introduced next. Among these approaches, physics-informed neural networks (PINNs) have emerged as particularly promising. PINNs integrate physical structure into learning and have been reported to improve fidelity and stability in geophysical settings (Raissi et al. 2019; Kharazmi et al. 2021; Wu et al. 2022; Karniadakis et al. 2021). Rather than enforcing a full heat-equation PDE, the present study adopts a lightweight temporal smoothness prior implemented as a finite difference on same-pixel pairs, ΔT/Δt to discourage unrealistically rapid day-to-day changes in predicted LST while keeping the network compact. As an urban example,(Chen et al. 2022) combined point-cloud information with physical constraints to model urban surface temperatures at high resolution (reporting R^2 up to 0.99). Although deep and hybrid learning has been widely explored for urban LST/UHI, few studies couple physics-based constraints with multitemporal, multisource inputs under a single city-scale pipeline, and even fewer conduct a like-for-like cross-city comparison across different climate regimes.

The present work introduces a lightweight PINN framework that combines Landsat-8–derived spectral indices, meteorological variables (temperature, humidity, solar radiation), and a digital elevation model (DEM) to predict 30-m LST in NYC and Austin two cities with different climate regimes. Lightweight denotes a shallow, computationally efficient network. Rather than enforcing a full heat-equation PDE, the model uses a minimal temporal smoothness prior a finite-difference term ΔT/Δt on same-pixel pairs to discourage unrealistically rapid day-to-day changes while preserving model compactness. The framework

---

[*] Corresponding author

This contribution has been peer-reviewed. The double-blind peer-review was conducted on the basis of the full paper.
https://doi.org/10.5194/isprs-annals-X-4-W8-2025-277-2026 | © Author(s) 2026. CC BY 4.0 License.

enables a unified cross-city comparison of LST drivers under consistent inputs and preprocessing.

2. STUDY AREA AND DATASET

NYC and Austin were illustrated in Figure 1; Texas were chosen as representative urban regions from two different climatic zones. NYC, situated in the northeastern United States, exhibits a humid subtropical climate rasterized by hot, humid summers and cold, icy winters. Austin, located in central Texas, possesses a humid subtropical climate defined by extended, arid summers and mild to warm winters. The differing climatic profiles create an optimal setting for assessing the applicability of the proposed LST prediction system across various environmental situations (Peel et al. 2007).

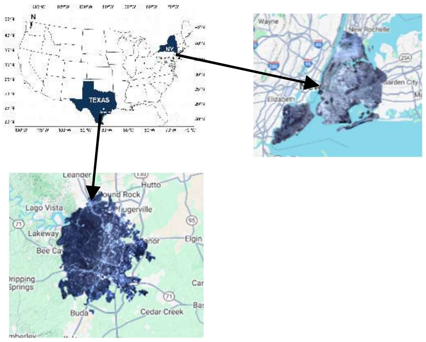

Figure 1. Study domains in New York City and Austin, Texas, illustrating the two contrasting urban test beds.

2.1 Data Sources

Spectral indices and LST were derived from Landsat-8 surface reflectance and thermal infrared data. Indices included NDVI, NDWI, NDBI/NDISI, and NDII, computed in Google Earth Engine (GEE) from Landsat-8 Collection 2 Level-2 surface reflectance (LANDSAT/LC08/C02/T1_L2). Thermal inputs were taken from the Landsat-8 Collection 2 Level-1 top-of-atmosphere dataset (LANDSAT/LC08/C02/T1_TOA) to retrieve LST from TIRS band 10 using single-channel, physics-based algorithms (Sobrino, Jiménez-Muñoz and Paolini, 2004, Li, Tang, Wu, Ren, Yan, Wan, Trigo and Sobrino, 2013) with emissivity estimated from NDVI-based schemes. Surface reflectance was atmospherically corrected by LaSRC. All imagery (May–September 2023; < 10% cloud cover) was temporally aligned to acquisition dates and synchronized with meteorological covariates obtained via the Visual Crossing Weather API (air temperature, relative humidity, shortwave radiation). All datasets were resampled and co-registered to a uniform 30 m grid (bilinear for continuous layers; nearest-neighbor for categorical masks); TIRS band-10 inputs (native 100 m) and retrieved LST were resampled to 30 m for map consistency. Reported metrics quantify in-sample fit to the satellite-retrieved LST target.

2.2 Target LST

The target variable is satellite-retrieved land surface temperature (LST) from Landsat-8 TIRS band 10, obtained via single-channel, physics-based algorithms with emissivity estimated from NDVI-based schemes (e.g., Sobrino et al., 2004; Li et al., 2013). No in situ LST ground truth was available; therefore, the reported metrics quantify in-sample fit to this satellite-based target. Pixels were quality-screened; temperatures are expressed in °C. TIRS band 10 is natively 100 m and was resampled to 30 m for consistency with the predictor grid. Scenes cover May–September 2023.

2.3 Predictors

Predictors include Landsat-derived indices (NDVI, NDWI, NDBI, NDII, NDISI), a digital elevation model (DEM), and meteorological variables (air temperature, relative humidity, shortwave radiation). Index definitions follow standard formulations; NDII is treated as a moisture-related index, and NDISI as an impervious/built-up proxy.

2.4 Masks and Harmonization

Cloud/shadow masks and invalid pixels were removed using product QA. All layers were co-registered to the LST grid and standardized using training-fold statistics.

3. METHODOLOGY

A PINN was used to estimate LST from multi-source predictors. The workflow follows Figure 2: Stage 1 (Datasets), Stage 2 (Preprocessing), Stage 3 (PINN Modeling), and Stage 4 (Training Evaluation and Outputs).

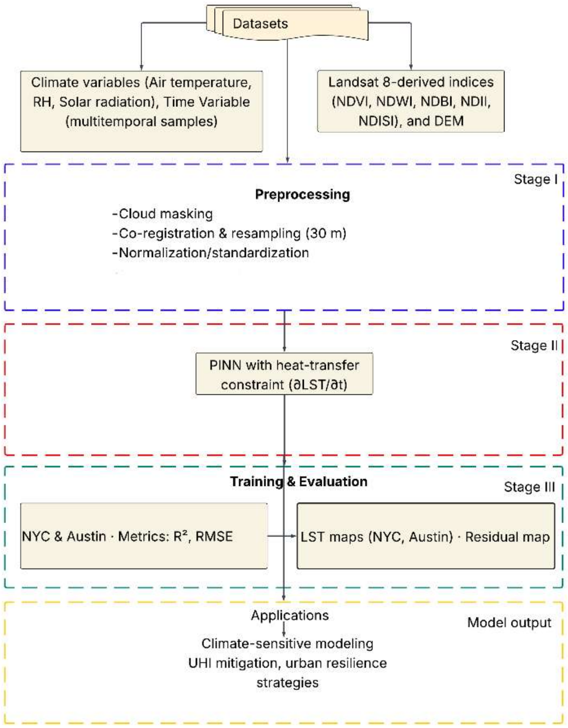

Figure 2. Workflow of the PINN framework.

3.1 PINN Architecture

The network comprises six residual blocks with 512 neurons per block. Each block uses the Swish activation to enhance nonlinearity while preserving smooth gradients. Batch normalization is applied before each block to stabilize learning, and dropout (rate = 0.2) follows each block to reduce overfitting. L2 weight decay (coefficient = 1×10^{-5}) regularizes parameter magnitudes. The input layer takes 12 standardized predictors: Landsat-derived spectral indices, a digital elevation model, meteorological variables (air temperature, relative humidity, shortwave radiation), and sinusoidal encodings of day-of-year.

https://doi.org/10.5194/isprs-annals-X-4-W8-2025-277-2026 |

The output layer contains a single linear neuron that yields LST (°C). This shallow configuration balances capacity and generalization and is readily combined with a temporal physics regularize during training.

3.2 Sampling and Batching

All QA-passed pixels from May–September 2023 were used on a common 30 m grid per city. Mini-batches were formed from non-overlapping spatial tiles to reduce local correlation during optimization; tiles were used only to form batches. When subsampling was required for efficiency, stratified random sampling by land-cover class preserved the representation of built-up, vegetation, and water. Features were standardized (mean, standard deviation) computed on the fitted set and applied unchanged, and day-of-year was encoded via sine and cosine for each pixel–date pair.

3.3 Training Setup

A fully connected PINN with six residual blocks (512 units per hidden layer) was optimized with Adam (learning rate = 1 × 10^{-3}). The learning rate was reduced on the training-loss plateau (factor 0.5, patience 5 epochs). Training used a fixed budget of up to 200 epochs (no validation-based early stopping). Dropout (0.2) followed each residual block, and L2 weight decay = 1 × 10^{-5} was applied. Mini-batches were randomly mixed across tiles and dates to stabilize gradient estimates; a typical mini-batch size of ≈1024 samples were used. Random seeds were fixed for data shuffling and parameter initialization to improve run-to-run reproducibility.

3.4 Loss Function

The objective combined a data term with a temporal physics term that reflects heat-storage behaviour:

$$\mathcal{L} = \frac{1}{N}\sum_{i=1}^{N}(T_i^{pred} - T_i^{LST})^2 + \lambda_{phys}\frac{1}{|P|}\sum_{(P,t)\in P}\left(\frac{T_{P,t+\Delta t_{P,t}}^{pred} - T_{P,t}^{pred}}{\Delta t_{P,t}}\right)^2 \quad (1)$$

Here, indexes all fitted (in-sample) pixels across dates; temperatures are in °C. P is the set of valid temporal pairs for the same pixel (p) where both dates pass QA. $\Delta t_{p,t}$ is the time gap in days between two successive acquisitions for that pixel (use a constant Δt if all gaps are equal). λ_{phys} is a dimensionless weight that balances the temporal smoothness with the data MSE. Pairs (t, t+Δt) are formed only when both dates for a pixel pass QA, encouraging physically plausible, day-to-day evolution (heat-storage behaviour). We tested $\lambda_{phys} \in \{0, 0.05, 0.1, 0.2, 0.5\}$ and $\lambda_{phys} = 0.2$ after a small in-sample grid search (smallest value that preserved or improved error while smoothing temporal residuals).

3.5 Evaluation Metrics

Model quality was summarized in-sample using the coefficient of determination (R^2) and root-mean-square error (RMSE, °C). Parity plots show predicted versus target values with a 1:1 line; residual maps use a symmetric colour scale in °C (default limits ±4 °C). Feature influence is reported using in-sample permutation importance. Unless noted, all metrics are computed over all QA-passed pixels for each city. For completeness, the metrics are:

$$RMSE = \sqrt{\frac{1}{N}\sum_{i=1}^{N}(T_i^{pred} - T_i^{LST})^2} \quad (2)$$

$$R^2 = 1 - \frac{\sum_{i=1}^{N}(T_i^{pred} - T_i^{LST})^2}{\sum_{i=1}^{N}(T_i^{LST} - \bar{T}^{LST})^2} \quad (3)$$

where N, number of samples; T_i^{pred} = predicted LST; T_i^{LST} satellite-retrieved LST; $\bar{T}^{LST}$ is mean target.

3.6 Training and Evaluation Protocol

Inputs are co-registered on the LST grid, shuffled, and batched. Standardization uses statistics computed on the training split only to prevent leakage. Optimization employs Adam with an initial learning rate of 1×10−3 and a decay schedule; early stopping monitors validation loss. Dropout (0.2) and L2 weight decay (1×10−5) act as regularizes. A fixed within-city holdout subset is reserved for each city and is used once for final reporting. Performance is summarized by coefficient of determination (R^2) and root-mean-square error (RMSE, °C) on the holdout. To support interpretation, feature importance is computed by permutation on the holdout. After convergence, the trained network is applied to all QA-passed pixels to generate city-scale LST and residual maps per date.

4. RESULT AND DISCUSSION

The performance of the PINN for NYC and Austin was evaluated on independent evaluation subsets for each city.

City	R^2	RMSE (°C)	Top influential Features
New York City	0.88	1.2	NDVI, Air Temperature
Austin, Texas	0.91	0.9	Solar Radiation, NDBI, NDISI

Table 1. Model performance and top influential features in NYC and Austin.

These results demonstrate robust accuracy for both cities. In New York City, NDVI and air temperature were the predominant variables, while in Austin, solar radiation and urban indices (NDBI, NDISI) were most influential. These findings underscore the need for climate-adapted modeling methodologies for mitigating urban heat.

4.1 New York City

Across NYC, predictions closely match measurements (R^2 = 0.88; RMSE = 1.2 °C). The point cloud is narrow and centered on the 1:1 line (Figure 3-a). Correlations (Figure 3-b) indicate modest positive associations for NDBI and NDVI, and weak negative associations for NDWI/NDWI_hum and NDISI, consistent with cooling by vegetation and moisture. DEM and spatial coordinates show near-zero correlations.

(a)

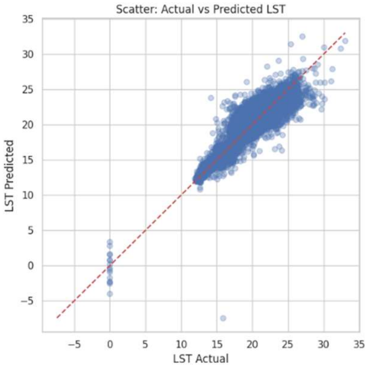

(b)

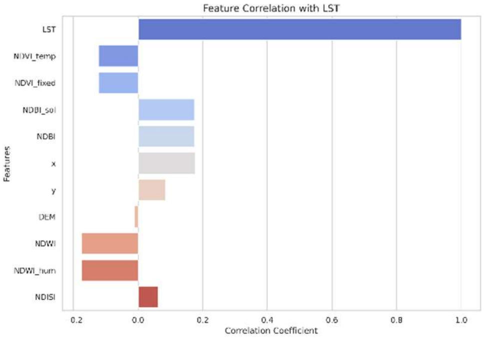

Figure 3. Scatter and correlation plots for NYC

4.2 Austin City

The model for Austin achieved an R^2 of 0.91 and an RMSE of 0.9 °C. Predicted values exhibit close grouping around the 1:1 line (Figure 4-a). The correlation results indicate solar radiation (r ≈ 0.39) and NDBI (r ≈ 0.22) as principal positive drivers of LST, while NDVI shows a negative (cooling) effect (Figure 4-b).

(a)

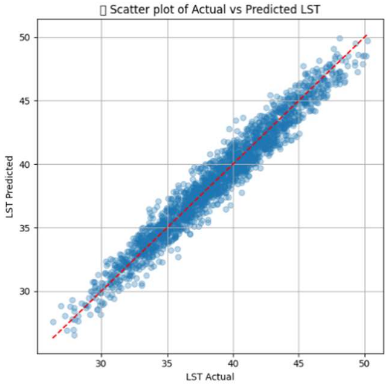

(b)

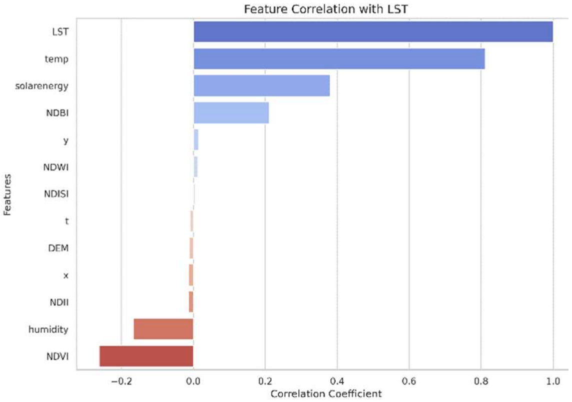

Figure 4. *Scatter and correlation plots for Austin*

4.3 Residual Analysis and Visual Evaluation

Residuals (Observed − Predicted) were computed pixel-wise across ≈ 1.14 million QA-passed pixels in the Austin study area (30 m grid; in-sample). The distribution is centered near zero (mean ≈ +0.0008 °C) with limited spread (SD ≈ 1.00 °C) and symmetric tails within ±4 °C, indicating spatially coherent, low-noise errors rather than random speckle.

(a)

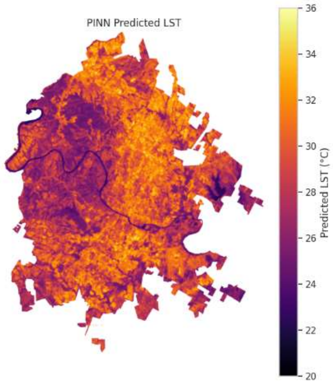

(b)

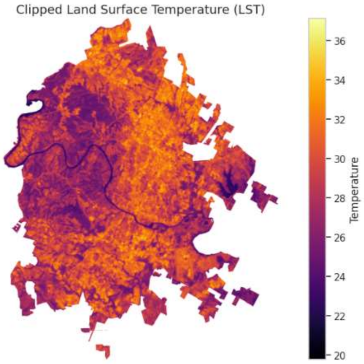

(c)

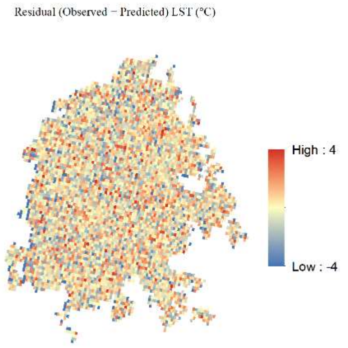

Figure 5. (a) Ground-truth LST, (b) PINN-predicted LST, and (c) residual map for Austin.

Alongside the statistical analysis, Figure 5 displays three separate thermal maps: Land Surface Temperature Estimated from Satellite, the estimated LST utilizing PINN, and the distribution of residuals. The agreement between actual and predicted maps, along with minimal residual magnitudes, illustrates substantial trustworthiness of the model in urban climate modeling tasks. Residual analysis is conducted for Austin as a representative instance due to its intricate climatic fluctuation and more irregular dataset, which caused significant challenges during model training. A similar assessment was conducted for NYC, where the more gradual convergence and reduced data variance yielded similarly consistent results. Comprehensive residual diagnostics for NYC will be supplied in forthcoming extensions.

Mean residual (℃)	Std Dev (℃)	Valid pixels count
0.00081	1.00162	1,140,000

Table 2. Residual statistics of LST prediction using PINN model in Austin.

Across NYC, the PINN reproduces the expected urban thermal pattern: dense built-up cores are warmer, while waterfronts and vegetated zones are cooler. Residuals are predominantly small, without large coherent error patches; positive speckles concentrate over intensely urbanized blocks and negative ones appear along water/park boundaries—consistent with mixed pixels (Figure 6). Table 3 reports residual statistics over the evaluation subset (n = 39,127; ≈ 4.4% of study-area valid pixels, n = 897,835); these counts reflect evaluation coverage, not city size. The near-zero mean bias and modest dispersion in Table 3 align with the spatial patterns observed in Figure 6.

(a)

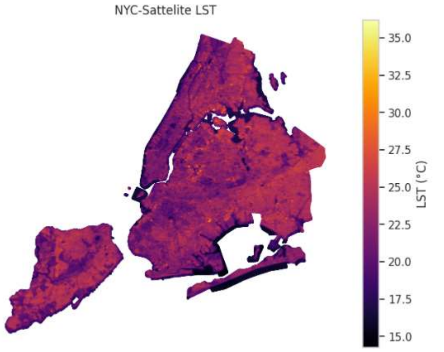

(b)

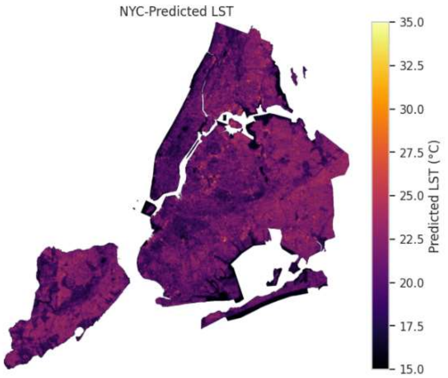

(c)

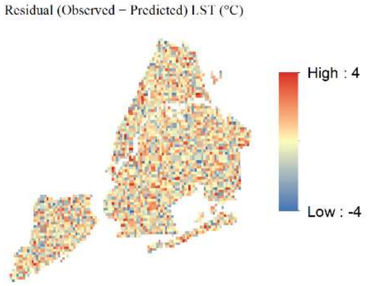

Figure 6. (a) Ground-truth LST, (b) PINN-predicted LST, and (c) residual map for New York.

Mean residual (℃)	Std Dev (℃)	Valid pixels count
0.0668	1.21115	897,835

Table 3. Residual statistics of LST prediction using PINN model in NYC.

4.4 Comparative Analysis

The findings suggest that factor importance varies with urban climatic context. In NYC, NDVI shows the strongest association with lower LST, while other spectral indices such as NDBI and DEM have moderate effects. Austin exhibits stronger influence from solar radiation and NDISI, consistent with the hotter, drier climate. Incorporation of the temporal physics constraint improves generalization and consistency across both locations. Despite mild fluctuations, the NYC model converged rapidly overall, whereas Austin exhibited larger oscillations in the loss, reflecting higher data variability and climatic complexity.

4.5 Training and Loss Dynamic Plots

Training-loss trajectories for NYC (top) and Austin (bottom) illustrate the behavior of the PINN under identical architectures and hyperparameters. In NYC, the loss decreases smoothly and then stabilizes, indicating stable optimization. In Austin, the loss converges to a similar level but with stronger epoch-to-epoch fluctuations, which is attributed to noisier gradients and higher data heterogeneity rather than optimizer instability. Both runs show stable convergence without divergence or clear overfitting signatures.

(NYC)

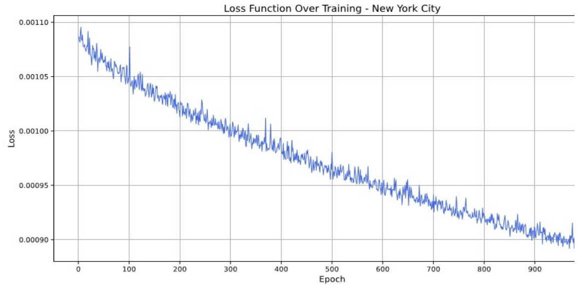

(Austin)

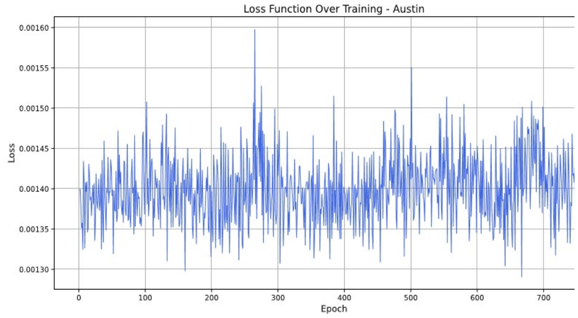

Figure 7. Training loss curves for the PINN model in NYC and Austin, showing convergence trends across epoch.

5. CONCLUSION

Reported accuracy levels in New York City ($R^2 = 0.88$; RMSE = 1.2 °C) and Austin ($R^2 = 0.91$; RMSE = 0.9 °C) quantify in-sample fit to a satellite-retrieved LST target at 30 m. Training-loss trajectories were smooth and near-monotonic in NYC, with larger oscillations in Austin. Correlation/permutation patterns indicated climate-dependent drivers: vegetation signals (e.g., NDVI) showed a cooling association in NYC, moisture-related indices (NDWI/NDII) were negatively associated with LST, while impervious-surface proxies (NDBI/NDISI) and shortwave/solar radiation exhibited stronger positive influence in Austin; NDVI retained a moderate cooling effect there. Residuals in both cities were approximately Gaussian with minimal bias, suggesting spatially coherent, low-noise errors. Incorporating a lightweight temporal smoothness term that penalizes day-to-day changes improved temporal coherence without additional architectural complexity, enabling a compact network suitable for routine city-scale mapping. Indicative implications are consistent with these patterns: in humid settings (e.g., NYC), strengthening vegetative cover is expected to yield larger cooling benefits, whereas in Austin (humid subtropical), managing radiative exposure and impervious surfaces appears more impactful.

This study is reported under a satellite-supervised setting; metrics quantify in-sample fit to a Landsat-8 single-channel LST target. Independent ground LST was unavailable, and 2-m air temperature records are not a direct reference for skin temperature. The analysis covers clear-sky scenes from May–September 2023 only; behaviour in other seasons and during extreme events may differ. TIRS band 10 (native 100 m) was resampled to 30 m; together with emissivity assumptions, atmospheric correction, BRDF effects, and mixed pixels, this may introduce retrieval bias. Despite tile-based batching to reduce local correlation, residual spatial autocorrelation may remain and inflate apparent accuracy. Feature attribution relies on in-sample permutation importance and is correlational rather than causal. Cross-city transfer and out-of-sample generalization were not assessed. Future work will incorporate leakage-aware spatial cross-validation, comparisons to independent skin-temperature products and site-level radiometry, multi-season evaluation, and uncertainty quantification (e.g., ensembles or probabilistic PINNs).

REFERENCES

Z. Qin, G. Dall'Olmo, A. Karnieli, P. Berliner, 2001: Derivation of split window algorithm and its sensitivity analysis for retrieving land surface temperature from NOAA-advanced very high resolution radiometer data. *Journal of Geophysical Research: Atmospheres*, 106, 22655-22670. doi.org/10.1029/2000JD900452.

J. A. Sobrino, J. C. Jiménez-Muñoz, L. Paolini, 2004: Land surface temperature retrieval from LANDSAT TM 5. *Remote Sensing of environment*, 90, 434-440. doi.org/10.1016/j.rse.2004.02.003.

Q. Weng, 2009: Thermal infrared remote sensing for urban climate and environmental studies: Methods, applications, and trends. *ISPRS Journal of photogrammetry and remote sensing*, 64, 335-344. doi.org/10.1016/j.isprsjprs.2009.03.007.

L. Zhu, G. I. Webb, M. Yebra, G. Scortechini, L. Miller F. Petitjean, 2021: Live fuel moisture content estimation from MODIS: A deep learning approach. *ISPRS Journal of Photogrammetry and Remote Sensing*, 179, 81-91. doi.org/10.1016/j.isprsjprs.2021.07.010.

A. A. Tehrani, O. Veisi,Y. Delavar, S. Bahrami, S. Sobhaninia A. Mehan, 2024: Predicting urban Heat Island in European cities: A comparative study of GRU, DNN, and ANN models using urban morphological variables. *Urban Climate*, 56, 102061. doi.org/10.1016/j.uclim.2024.102061.

Q. Weng, D. Lu J. Schubring, 2004: Estimation of land surface temperature–vegetation abundance relationship for urban heat island studies. *Remote sensing of Environment*, 89, 467-483. doi.org/10.1016/j.rse.2003.11.005.

J. Zhou, X. Zhang,W. Zhan, H. Zhang, 2014: Land surface temperature retrieval from MODIS data by integrating regression models and the genetic algorithm in an arid region. *Remote Sensing*, 6, 5344-5367. doi.org/10.3390/rs6065344.

Z. W. Zhou WeiQi,W. J. Wang Jia M. Cadenasso, 2017: Effects of the spatial configuration of trees on urban heat mitigation: a comparative study. *Remote Sensing of Environment*. doi.org/10.1016/j.rse.2017.03.043.

G. Zhao,Y. Zhang, J. Tan,C. Li Y. Ren, 2020: A data fusion modeling framework for retrieval of land surface temperature from Landsat-8 and MODIS Data. *Sensors*, 20, 4337. doi.org/10.3390/s20154337.

F. Liu, X. Zhang,Y. Murayama T. Morimoto, 2020: Impacts of land cover/use on the urban thermal environment: a comparative study of 10 megacities in China. *Remote Sensing*, 12, 307. doi.org/10.3390/rs12020307.

B. Singh, G. Paudel, A. Thapa, H. C. Joshi M. Maharjan, 2024: Urban heat island relation with land use land cover change in Hetauda sub-metropolitan city of Nepal. *Archives of Agriculture and Environmental Science*, 9, 691-698. doi.org/10.26832/24566632.2024.090408.

Z. Dai, J.-M. Guldmann Y. Hu, 2018: Spatial regression models of park and land-use impacts on the urban heat island in central Beijing. *Science of the total environment*, 626, 1136-1147. doi.org/10.1016/j.scitotenv.2018.01.165.

R. Ghanbari, M. Heidarimozaffar, A. Soltani, H. Arefi, 2023: Land surface temperature analysis in densely populated zones from the perspective of spectral indices and urban morphology. *International Journal of Environmental Science and Technology*, 20, 2883-2902. doi.org/[10.1007/s13762-022-04725-4.

F. Johannsen, P. M. Soares G. S. Langendijk, 2024: On the Deep learning approach for improving the representation of urban climate: the Paris urban heat island and temperature extremes. *Urban Climate*, 56, 102039. doi.org/10.1016/j.uclim.2024.102039.

M. Raissi, P. Perdikaris, G. E. Karniadakis, 2019: Physics-informed neural networks: A deep learning framework for solving forward and inverse problems involving nonlinear partial differential equations. *Journal of Computational physics*, 378, 686-707. doi.org/10.1016/j.jcp.2018.10.045.

E. Kharazmi, M. Cai, X. Zheng, Z. Zhang, G. Lin G. E. Karniadakis, 2021: Identifiability and predictability of integer- and fractional-order epidemiological models using physics-informed neural networks. *Nature Computational Science*, 1, 744-753. doi.org/[10.1038/s43588-021-00158-0
.

D. Wu,W. Liu, B. Fang, L. Chen,Y. Zang, L. Zhao, S. Wang, C. Wang, J. Marcato J. Li, 2022: Intracity temperature estimation by physics informed neural network using modeled forcing meteorology and multispectral satellite imagery. *IEEE Transactions on Geoscience and Remote Sensing*, 60, 1-15. doi.org/[10.1109/TGRS.2022.3201284.

G. E. Karniadakis, I. G. Kevrekidis, L. Lu, P. Perdikaris, S. Wang L. Yang, 2021: Physics-informed machine learning. *Nature Reviews Physics*, 3, 422-440. doi.org/[10.1038/s42254-021-00314-5.

L. Chen, B. Fang, L. Zhao,Y. Zang,W. Liu,Y. Chen, C. Wang J. Li, 2022: DeepUrbanDownscale: A physics informed deep learning framework for high-resolution urban surface temperature estimation via 3D point clouds. *International Journal of Applied Earth Observation and Geoinformation*, 106, 102650. doi.org/[https://doi.org/10.1016/j.jag.2021.102650.

M. C. Peel, B. L. Finlayson, T. A. McMahon, 2007: Updated world map of the Köppen-Geiger climate classification. *Hydrology and earth system sciences*, 11, 1633-1644. doi.org/10.5194/hess-11-1633-2007.

Z.-L. Li, B.-H. Tang, H. Wu, H. Ren, G. Yan, Z. Wan, I. F. Trigo J. A. Sobrino, 2013: Satellite-derived land surface temperature: Current status and perspectives. *Remote sensing of environment*, 131, 14-37. doi.org/10.1016/j.rse.2012.12.008.